

Hydrolysis kinetic study of $\text{CaAlSiN}_3:\text{Eu}^{2+}$ red phosphor with both water immersion test and first-principles calculation

Fan, Jiajie; Zhou, Ling; Cui, Zhen; Chen, Shanghuan; Fan, Xuejun; Zhang, Guoqi

DOI

[10.1016/j.jlumin.2019.116874](https://doi.org/10.1016/j.jlumin.2019.116874)

Publication date

2020

Document Version

Final published version

Published in

Journal of Luminescence

Citation (APA)

Fan, J., Zhou, L., Cui, Z., Chen, S., Fan, X., & Zhang, G. (2020). Hydrolysis kinetic study of $\text{CaAlSiN}_3:\text{Eu}^{2+}$ red phosphor with both water immersion test and first-principles calculation. *Journal of Luminescence*, 219, 1-11. Article 116874. <https://doi.org/10.1016/j.jlumin.2019.116874>

Important note

To cite this publication, please use the final published version (if applicable). Please check the document version above.

Copyright

Other than for strictly personal use, it is not permitted to download, forward or distribute the text or part of it, without the consent of the author(s) and/or copyright holder(s), unless the work is under an open content license such as Creative Commons.

Takedown policy

Please contact us and provide details if you believe this document breaches copyrights. We will remove access to the work immediately and investigate your claim.



Hydrolysis kinetic study of $\text{CaAlSiN}_3:\text{Eu}^{2+}$ red phosphor with both water immersion test and first-principles calculation

Jiajie Fan^{a,b,c,*}, Ling Zhou^{a,b}, Zhen Cui^c, Shanghuan Chen^{a,b}, Xuejun Fan^d, Guoqi Zhang^c

^a College of Mechanical and Electrical Engineering, Hohai University, Changzhou, 213022, China

^b Changzhou Institute of Technology Research for Solid State Lighting, Changzhou, 213161, China

^c Department of Microelectronics, EEMCS Faculty, Delft University of Technology, Delft, 2628, the Netherlands

^d Department of Mechanical Engineering, Lamar University, Beaumont, TX, 77710, USA

ARTICLE INFO

Keywords:

$\text{CaAlSiN}_3:\text{Eu}^{2+}$

Hydrolysis kinetic

Water immersion test

First-principles

Reliability

ABSTRACT

At present, most high-power white Light-emitting diode and laser diode (LED&LD) package is usually constructed by a blue LED&LD chip with a Cerium doped Yttrium Aluminum Garnet (YAG:Ce³⁺) yellow phosphor, but its color rendering performance is severely challenged due to the lack of red light emission spectrum. The $\text{CaAlSiN}_3:\text{Eu}^{2+}$ red phosphor can effectively improve the color quality of traditional yellow phosphor converted white LED&LDs (pc-wLED&LDs), however, it is often susceptible to degradation under high temperature and high humidity environments, which will directly affect the color quality of pc-wLED&LDs. In this study, a series of water immersion tests on $\text{CaAlSiN}_3:\text{Eu}^{2+}$ red phosphor are used to quantitatively study its hydrolysis reaction kinetics. Then, the degradations of its photoluminescence and photothermal performances are evaluated by characterizing the crystal structure, micromorphology and chemical element composition. Finally, an atomic level hydrolysis reaction mechanism of $\text{CaAlSiN}_3:\text{Eu}^{2+}$ red phosphor is investigated by using the first-principles density functional theory (DFT) calculation. The results show that: (1) By modelling the in-situ monitored electrical conductivity of $\text{CaAlSiN}_3:\text{Eu}^{2+}$ red phosphor water solution with a first-order reaction function, the calculated hydrolysis reaction rate satisfies the Arrhenius relationship and the reaction activation energy is estimated as 49.19 kJ/mol; (2) The increased self-heating effect of $\text{CaAlSiN}_3:\text{Eu}^{2+}$ red phosphor after water immersion test attribute to its drastic drop of light emission efficiency; (3) The hydrolysis reaction mechanism of $\text{CaAlSiN}_3:\text{Eu}^{2+}$ red phosphor is confirmed, which sequentially results in the dissolution of Ca^{2+} and OH^- , the crash of host lattice and the accumulation of reaction residues.

1. Introduction

Due to their lower energy consumption, long lifetime, fast response and compact size, high-power white Light-emitting diode and laser diode (LED&LD) are becoming one of new generation light sources used in indoor and outdoor lighting, automotive lamps, displays and light healthcare etc. [1,2] With the increase of living quality, people's requirement on lighting has gradually shifted from the higher light-output and low power consumption to the more healthy and comfortable lighting quality [3–5]. At present, a commonly used high-power phosphor-converted white LED&LDs (pc-wLED&LDs) is usually composed by a blue LED&LD chip coated with phosphor materials. As one of critical light-conversion components, phosphors always determine the light efficacy and quality of high-power pc-wLED&LDs

[6]. The traditional pc-wLED&LD coated with the Cerium doped Yttrium Aluminum Garnet (YAG:Ce³⁺) yellow phosphor, with an emission spectrum mainly located around yellow-green, has been considered as one of most effective ways to produce white light [7]. The optical performance YAG:Ce³⁺ yellow phosphor-converted white LED has been accurately characterized and modelled by R. Hu and X.B. Luo [8–10]. However, due to the deficiency of red color component, the final packaged white LED&LD with yellow phosphor has a low color rendering index (CRI) and high correlated color temperature (CCT), that becomes the bottleneck of application in high lighting quality field [11]. The addition of red phosphor can effectively improve the color-rendering and reduce the color temperature of traditional YAG based pc-wLED&LDs, and its prominent role has gradually become a research focus in pc-wLED&LD's phosphors [12,13]. Traditionally, red

* Corresponding author. College of Mechanical and Electrical Engineering, Hohai University, Changzhou, 213022, China.

E-mail addresses: jay.fan@connect.polyu.hk, jiajie.fan@hhu.edu.cn (J. Fan).

<https://doi.org/10.1016/j.jlumin.2019.116874>

Received 19 August 2019; Received in revised form 28 October 2019; Accepted 4 November 2019

Available online 7 November 2019

0022-2313/© 2019 Elsevier B.V. All rights reserved.

phosphors, such as Eu^{2+} doped sulfide and Mn^{4+} doped fluoride systems, are prepared with hydrogen sulfide atmosphere and hydrofluoric acid respectively with the complicated process. Their physical and chemical properties are unstable and deliquescent [14]. After that, the Eu^{2+} doped Nitride red phosphors, such as $\text{CaAlSiN}_3:\text{Eu}^{2+}$, $\text{SrAlSiN}_3:\text{Eu}^{2+}$, $\text{Ba}_2\text{AlSi}_5\text{N}_9:\text{Eu}^{2+}$, etc., with high quantum yield, good chemical and thermal stability and no pollutant release during production, are developed for white LED&LDs with wide color gamut [15].

As a critical light-conversion component, phosphor's stability will directly affect the reliability of pc-wLED&LD package [16,17]. In the actual application, the temperature at which the LED&LD chip works is high [18], and the phosphor may undergo thermal quenching to cause a change of luminous intensity or peak wavelength, resulting in the lumen degradation and color shift of pc-wLED&LDs [7]. Moreover, besides the high temperature, humidity is considered as another factor to induce the degradation of phosphor, and finally deteriorate the optical intensity and color quality of pc-wLED&LDs [19,20]. Thus, the stability and reliability assessment on phosphors under high humidity condition has attracted more interests from pc-wLED&LD research and industry. For example, M. Choi et al. [21] used the pH change of phosphor solution to evaluate its reactivity with water, and correlated this test with its long-term reliability. C. F. Guo et al. [22] studied the hydrolysis process of $\text{SrAl}_2\text{O}_4:\text{Eu}^{2+},\text{Dy}^{3+}$ green phosphor and found that it was extremely unstable to water and moisture, and its hydrolysis product included suspended layer and sediment. W. X. Li et al. [23] revealed that the luminescence intensity of narrow-band red-emitting $\text{SrLiAl}_3\text{N}_4:\text{Eu}^{2+}$ phosphor was almost disappeared after being treated at 100% humidity for 72 h. The color of phosphor was gradually bleached, and the rod shape residues after degradation were completely split. J. J. Fan et al. [24] found that phosphors reacted with water and produced OH^- to increase the pH value under hydrothermal environment, that confirmed the hydrolysis reaction of phosphors in the water immersion test. The performance change of treated phosphors also kept consistent with the long-term high temperature and high humidity aging test results of both phosphor itself and phosphor/silicone composite [19,25,26]. Therefore, some solutions to improve the phosphor's moisture-resistance have been proposed by modifying the activator ion [27] and surface [28].

$\text{CaAlSiN}_3:\text{Eu}^{2+}$ has been considered as one of most successfully commercialized red phosphor products used in high-color-rendering LED&LD lighting and display [29–34]. It was firstly developed by K. Uheda et al. [35] under a high-temperature and high-pressure solid state reaction with EuN , Ca_3N_2 , AlN and Si_3N_4 . According to the effective first-principles calculation, the host lattice constants [36,37] and mechanical, electrical and optical properties [38] of $\text{CaAlSiN}_3:\text{Eu}^{2+}$ red phosphor and its derivatives [39,40] were predicted. However, although it has a high thermal quenching temperature and good thermal stability [41], the reliability of $\text{CaAlSiN}_3:\text{Eu}^{2+}$ red phosphor is still being challenged by the high humidity application condition [41–43]. J. Zhu et al. [42] developed a high-pressure water stream test to analyze the moisture driven degradation mechanism of $(\text{Sr}, \text{Ca})\text{AlSiN}_3:\text{Eu}^{2+}$ red phosphor, in which the oxidation of both the phosphor host and activator with an oxidant-gas penetration was considered as the root cause. Our research team also experimentally found the hydrolysis phenomenon of $\text{CaAlSiN}_3:\text{Eu}^{2+}$ red phosphor and its interaction with silicone under long-term high temperature and high humidity ageing test [19,25]. However, all current understandings of hydrolysis reaction of $\text{CaAlSiN}_3:\text{Eu}^{2+}$ red phosphor rely on the characterizations of microstructure and chemical element composition, that can't provide a deep understanding at atomic level.

In this paper, we investigate the hydrolysis reaction mechanism of $\text{CaAlSiN}_3:\text{Eu}^{2+}$ red phosphor by implementing a self-designed water immersion test and the first-principles density functional theory (DFT) calculation. As shown in Fig. 1, to understand the high humidity driven degradation mechanism of $\text{CaAlSiN}_3:\text{Eu}^{2+}$ red phosphor, a water immersion test under temperatures from 30 to 55 °C was firstly designed to simulate a high humidity and ambient temperature storage condition.

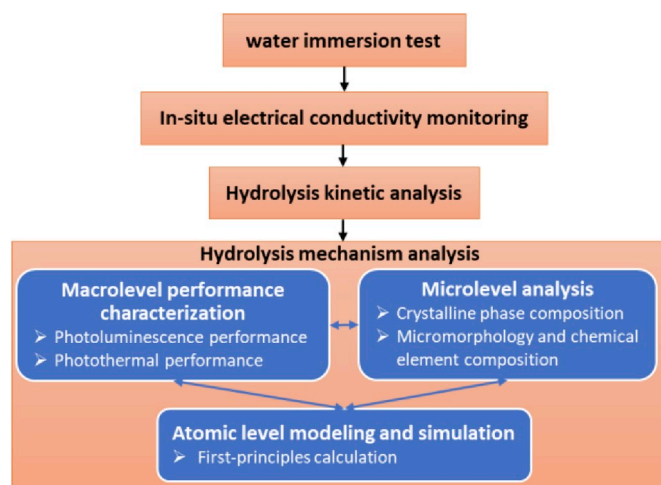


Fig. 1. The logic and organization of this study.

Then, a quantitatively kinetic study of hydrolysis reaction mechanism was conducted. Next, the photoluminescence and photothermal properties of phosphors before and after test were compared and explained by analyzing the crystal structure, microscopic surface morphology and composition via X-ray Diffraction (XRD), Scanning Electron Microscopy (SEM) and Energy Dispersive Spectroscopy (EDS) respectively. Finally, the first-principles calculation was used to understand this hydrolysis reaction mechanisms at the atomic level.

2. Test sample and experiment

A commercialized $\text{CaAlSiN}_3:\text{Eu}^{2+}$ red phosphor product is selected in this study. As shown in Fig. 2, the host lattice CaAlSiN_3 has an orthorhombic crystal structure (space group $\text{Cmc}2$, no. 36), in which Ca atoms occupy the vacancies within the six corner-connected $\text{SiN}_4/\text{AlN}_4$ tetrahedra [37,40].

2.1. Water immersion test setup and experimental procedure

As shown in Fig. 3, the water immersion test setup includes an electrical conductivity monitor (Model: DDS-307) and a water-bath heater system with the constant temperature controller and magnetic stirrer (Model: DF-101SZ). The experimental procedure of preparing test samples includes: firstly, 10 g red phosphor powders were weighted and poured with 100 ml deionized water in a beaker; Then, the beaker was put into the water-bath heater system and set the treatment temperatures from 30 to 55 °C with a 5 °C increment. The rotation speed of

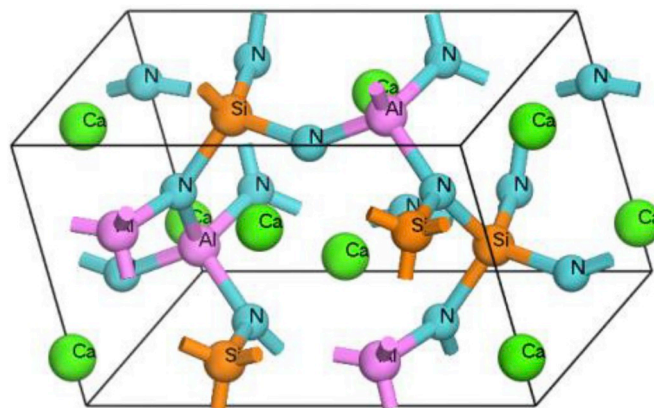


Fig. 2. The host lattice structure of CaAlSiN_3 .

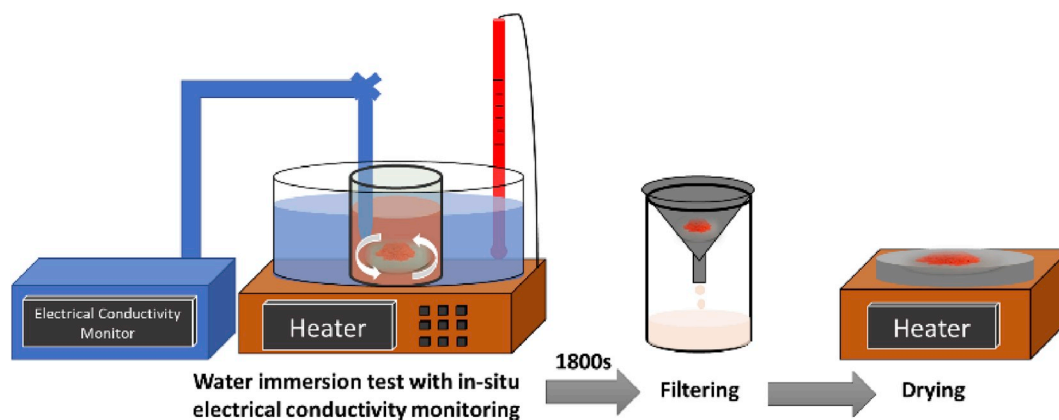


Fig. 3. Experimental procedure of the designed water immersion test.

magnetic stirrer was set as 450 rpm to ensure an even reaction; Next, the electrical conductivity was in-situ monitored for the phosphor water solution when the solution temperature was stably controlled, and the recording cycle of electrical conductivity was set as 20s until 1800s; Finally, the phosphor powders after water immersion test were filtered and dried from solution for the next step's performance characterization.

2.2. Material characterization

The photoluminescence performance and thermal stability of $\text{CaAlSi}_3\text{Eu}^{2+}$ red phosphors were characterized by using the Exciting Spectra and Thermal Quenching Analyzer from the EVERFINE Corporation (Model: EX-1000). Their photothermal characterizations were measured by using a home-made infrared imaging system as described in Fig. 8. The crystalline phase composition was detected by the X-ray Diffractometry (XRD, Rigaku D/MAX 2500 V/PC, Japan). The surface morphology was observed by the Scanning Electron Microscopy (SEM, JEOL/JSM-6510, Japan). The Energy Dispersive Spectroscopy (EDS, JEOL/Ex-54175JMU, Japan) was used to analyze the types and contents of chemical elements.

3. Results and discussion

3.1. Hydrolysis kinetic analysis

Fig. 4 shows the in-situ monitored electrical conductivity of $\text{CaAlSi}_3\text{Eu}^{2+}$ red phosphor water solution and their nonlinear fitting results at different temperatures. It can be seen that the electrical conductivity of $\text{CaAlSi}_3\text{Eu}^{2+}$ red phosphor water solution increased rapidly in the initial 200 s, then went saturated. When the rising of solution temperature, the electrical conductivity gradually increased, indicating that high temperature can promote the dissolution of $\text{CaAlSi}_3\text{Eu}^{2+}$ red phosphor in water. All electrical conductivities can be fitted by the exponential function with assumption of following the first-order reaction.

For the first-order reaction, the relationship between reaction rate k and water immersion test temperature T follows the Arrhenius equation, as shown in equations (1) and (2) [42]:

$$k = A \cdot \exp\left(\frac{E_a}{RT}\right) \quad (1)$$

$$\ln k = -\frac{E_a}{RT} + \ln A \quad (2)$$

Where A is a pre-factor; R is the gas constant, $8.314 \text{ J}/(\text{mol}\cdot\text{K})$; T is the thermodynamic temperature, K ; E_a is the activation energy, kJ/mol .

Then, the reaction rates at different temperatures are obtained from

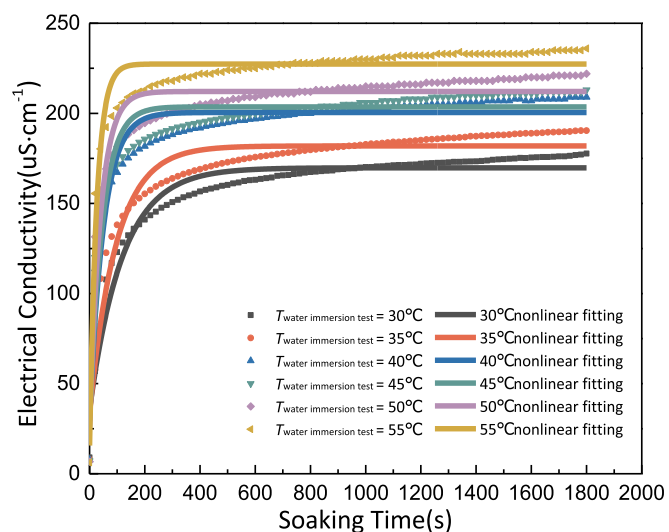


Fig. 4. Electrical conductivity v.s. temperature of $\text{CaAlSi}_3\text{Eu}^{2+}$ red phosphor water solution and the nonlinear fitting results. (For interpretation of the references to color in this figure legend, the reader is referred to the Web version of this article.)

fitting results and listed in Table 1. Fig. 5 shows that $\ln k$ and $1/T$ are linearly correlated, and can be modelled by the Arrhenius equation (2). The slope of linearly fitted curve from Fig. 4 can be calculated as the activation energy of hydrolysis reaction from 303 to 328 K, $E_a = 49.19 \text{ kJ}/\text{mol}$.

3.2. Photoluminescence performance characterization

In this section, the Exciting Spectra and Thermal Quenching Analyzer were used to evaluate the photoluminescence performances of $\text{CaAlSi}_3\text{Eu}^{2+}$ red phosphors before and after the water immersion test. The thermal quenching test temperature was controlled from 40°C to

Table 1
The exponential fitting results of electrical conductivities.

$T_{\text{water immersion test}}/\text{K}$	k/s^{-1}	R [2]
303	0.00838	0.93542
308	0.01036	0.91308
313	0.01949	0.89067
318	0.0214	0.88225
323	0.0252	0.88457
328	0.03806	0.90868

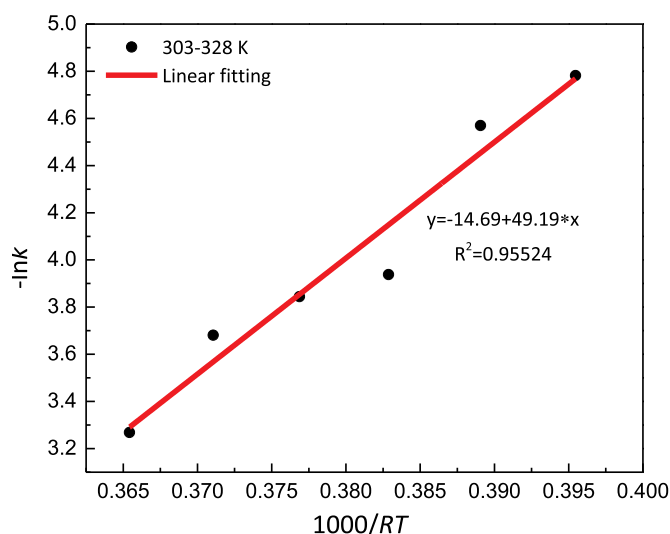


Fig. 5. The hydrolysis reaction rate v.s. temperature.

80 °C with a temperature interval as 10 °C.

3.2.1. Excitation spectrum v.s. thermal quenching test temperature

Fig. 6(a–f) shows the excitation spectra of $\text{CaAlSiN}_3:\text{Eu}^{2+}$ red phosphors treated under different thermal quenching test temperatures. It can be seen that when the temperature of water immersion test increased, the peak wavelength of excitation spectrum did not change too much, which was always around 475 nm. However, the temperature dependence of excitation intensity of phosphor after high temperature water treatment increased much more. This means that the hydrolysis reaction can influence the light absorption efficiency of $\text{CaAlSiN}_3:\text{Eu}^{2+}$ red phosphor, which may be attributed to the micromorphology deterioration of phosphor particles.

3.2.2. Emission spectrum v.s. thermal quenching test temperature

Subsequently, the thermal stability of $\text{CaAlSiN}_3:\text{Eu}^{2+}$ red phosphor

was characterized by comparing their emission spectra when the peak excitation wavelength was set as 475 nm. Three characteristics of emission spectrum, including Full Width at Half Maximum (FWHM), Peak Wavelength, and Emission Intensity, were extracted and their thermal quenching effects were collected and shown in Fig. 7(a–c).

As shown in Fig. 7(a), the FWHMs gradually became broader accompany with the raising of thermal quenching test temperature and the increment of FWHMs of samples soaked at different water temperatures kept relatively similar. This means that the color purity of $\text{CaAlSiN}_3:\text{Eu}^{2+}$ red phosphor deteriorates under high temperature treatment, but the hydrolysis reaction has less impact on it. The peak wavelength, determining the color fidelity, changed less when increase the water immersion test temperature as shown in Fig. 7(b). Meanwhile, the temperature stability of peak wavelength kept relatively well. Fig. 7 (c) presents that all peak intensities of $\text{CaAlSiN}_3:\text{Eu}^{2+}$ red phosphors after hydrolysis reaction were linearly degraded as a function of thermal quenching test temperature. At the same time, according to the increased slopes of linear-fitting curves, it can be seen that the water immersion test at higher temperature can accelerate the thermal quenching effect and quickly drop the emission efficiency of $\text{CaAlSiN}_3:\text{Eu}^{2+}$ red phosphor.

3.3. Photothermal performance characterization

Normally, the phosphor excited by the illumination will simultaneously converts the light and produces the heat, because of the Stokes effect. In this section, the photothermal effects of $\text{CaAlSiN}_3:\text{Eu}^{2+}$ red phosphors were characterized by using both the infrared thermal (IR) measurement and the finite element simulation. In Fig. 8, the photothermal test setup was designed by using an IR thermal camera, a blue LED driven by the controllable constant current, a light guide plate covered on the top of blue LED chip and a glass plate with a circular groove (with a depth of 0.2 mm and a diameter of 14 mm) filled by $\text{CaAlSiN}_3:\text{Eu}^{2+}$ red phosphor powders. The excitation lights were produced by the blue LED with different driven currents (i.e. 140 mA, 210 mA, 280 mA, 350 mA) and the phosphor samples before and after water immersion test were placed in the circular groove of glass piece for photothermal characterization. During the test, a thermal stabilization

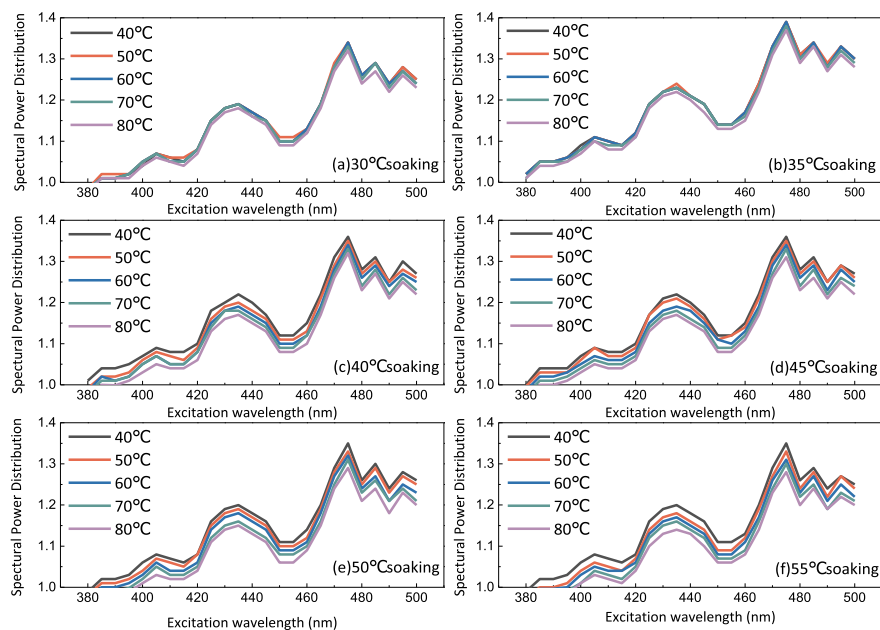


Fig. 6. Excitation spectrum v.s. thermal quenching test temperature of $\text{CaAlSiN}_3:\text{Eu}^{2+}$ red phosphor after the water immersion test at (a) 30 °C; (b) 35 °C; (c) 40 °C; (d) 45 °C; (e) 50 °C and (f) 55 °C. (For interpretation of the references to color in this figure legend, the reader is referred to the Web version of this article.)

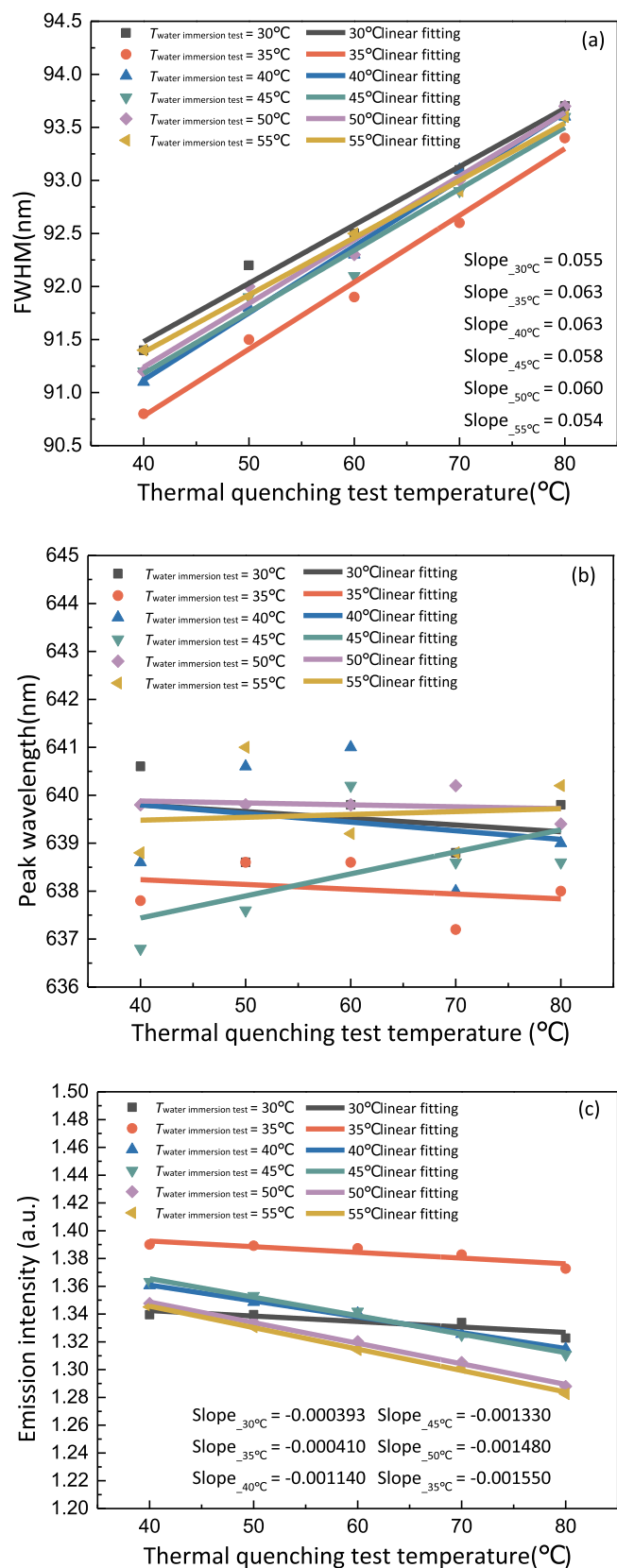


Fig. 7. Emission spectrum v.s. thermal quenching test temperature of CaAlSiN₃:Eu²⁺ red phosphor after the water immersion test (a) FWHM; (b) Peak wavelengths; (c) Emission intensity. (For interpretation of the references to color in this figure legend, the reader is referred to the Web version of this article.)

with 10–15 min was required before IR measurement. Table 2 compares the photothermal performances of CaAlSiN₃:Eu²⁺ red phosphor after 30 °C and 55 °C water immersion tests.

Fig. 9(a) plots the maximum surface temperatures of phosphor samples before and after water immersion test, in which the excitation lights were controlled by adjusting the driven current of blue LED. The results in Fig. 9(b) show that the averaged maximum surface temperatures of each test samples were linearly fitted as a function of driven current. It is also found that the temperature increment rate, that is represented by the linear curve slope, increased accompany with the rising of water immersion test temperature. These results keep corresponding with the drop of emission peak described in Fig. 7(c).

As a short summary, the above thermal measurement results indicate that the increase of excited blue light will promote the photothermal effect of phosphor to raise the surface temperature accordingly. In the meantime, the measured maximum surface temperatures of phosphors after water immersion test are all higher than those without test. The water treatment at higher temperature can accelerate the photothermal effect of the phosphor and increase its self-heating as its emission efficiency drop described in the above section. This phenomenon can be explained by the principle of energy conservation, the energy absorbed by phosphor is equal to the sum of the light energy emitted and the heat generated by phosphor, as described in equation (3).

$$Q_p = Q_l + Q_h \quad (3)$$

Where Q_p refers to the energy absorbed by phosphor; Q_l is the light energy emitted by phosphor; Q_h is the self-heating energy generated by phosphor.

Next, in order to understand the photo-induced self-heating phenomenon of CaAlSiN₃:Eu²⁺ red phosphor, its photothermal effect was simulated in this section with the finite element simulation. As shown in Fig. 10, a three-layer close-packed CaAlSiN₃:Eu²⁺ red phosphor particles can be simplified as a tetragonal microscopic basic unit. The macroscopic model is assumed as the accumulation of microscopic basic units regardless of defects and impurities. The microscopic model of a CaAlSiN₃:Eu²⁺ red phosphor particle is rod-shaped with r as its radius and l as its length, assuming $r = 10 \mu\text{m}$, $l = 50 \mu\text{m}$ in this study.

The effect of phosphor particle spacing (d) on the photothermal effect is discussed as follows according to the finite element thermal dissipation simulations. In detail, the temperature differences between the bottom of first layer and the top of third layer were simulated by setting the $d = 2.0r$, $2.5r$, $3.0r$ and $3.5r$ respectively. Fig. 11 shows the relationship between the simulated temperature difference and phosphor particle spacing. It is indicated that when the spacing of the phosphor particles increased, the effects of both the increased air resistance between particles and more excited phosphors resulted in an increase of temperature difference in the phosphor compact model. The relationship between the temperature difference and particle spacing can be quantified through fitting a logarithmic function as described in equation (4):

$$\Delta\text{Temp} = 2.67 \cdot \ln(d) - 7.34 \quad (4)$$

3.4. Crystalline phase composition analysis

In this section, X-ray diffraction (XRD) is used to analyze the crystal structures of CaAlSiN₃ host lattice before and after water immersion test as shown in Fig. 12.

Through comparing the diffraction peaks of standard card JCPDS#39-0747 [44–47], CaAlSiN₃ is considered as the principle crystalline phase even after water immersion tests. Table 3 compares four highest diffraction peak intensities before and after tests, it is found that although their diffraction peak intensities dramatically degraded after the water immersion test, the characteristic diffraction angles kept relatively stable. The highest diffraction peak at $\sim 36.6^\circ$ became broader and this means an amorphous trend happened in CaAlSiN₃ host lattice,

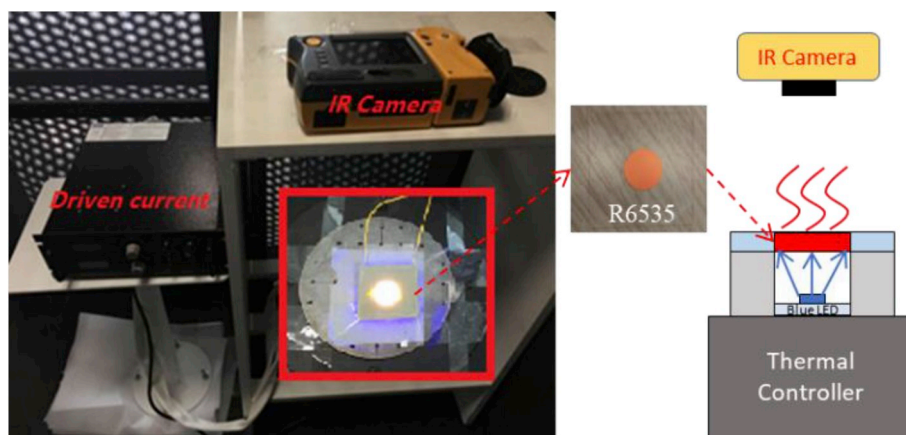


Fig. 8. The photothermal test setup for CaAlSiN₃:Eu²⁺ red phosphor. (For interpretation of the references to color in this figure legend, the reader is referred to the Web version of this article.)

Table 2
IR imaging of CaAlSiN₃:Eu²⁺ red phosphor after 30 °C and 55 °C water immersion tests.

Driven current of blue LED/mA	$T_{\text{water immersion test}} = 30^{\circ}\text{C}$	$T_{\text{water immersion test}} = 55^{\circ}\text{C}$
140	$T_{\text{max}}=26.1^{\circ}\text{C}$	$T_{\text{max}}=28.5^{\circ}\text{C}$
210	$T_{\text{max}}=29.0^{\circ}\text{C}$	$T_{\text{max}}=30.7^{\circ}\text{C}$
280	$T_{\text{max}}=30.8^{\circ}\text{C}$	$T_{\text{max}}=32.8^{\circ}\text{C}$
350	$T_{\text{max}}=32.3^{\circ}\text{C}$	$T_{\text{max}}=34.7^{\circ}\text{C}$

however, the new crystalline phase was difficultly identified in current XRD patterns [42]. Moreover, the temperature dependence of peak intensity can't be simply functioned like previous electrical conductivity, emission peak intensity and photothermal characteristic. This may reveal that the crystalline phase of CaAlSiN₃ host lattice is not the only determinative factor on phosphor's performance, the activator is another influence factor.

3.5. Micromorphology and chemical element composition analysis

Furthermore, SEM is used in this study to observe the changes of micromorphology of CaAlSiN₃:Eu²⁺ red phosphor particles before and after water immersion test. Meanwhile, the chemical element types and compositions of phosphor particles are analyzed by using the EDS measurements. Fig. 13 shows the SEM images of CaAlSiN₃:Eu²⁺ red phosphors treated under different water immersion temperatures. The results indicate that an increased surface roughness and new residues after hydrolysis reaction may correspond to the reduction of XRD peak intensity. But the cracks and wrinkles on the particle surface happened in Ref [42]⁴² were not found in our test, this may relate to the different

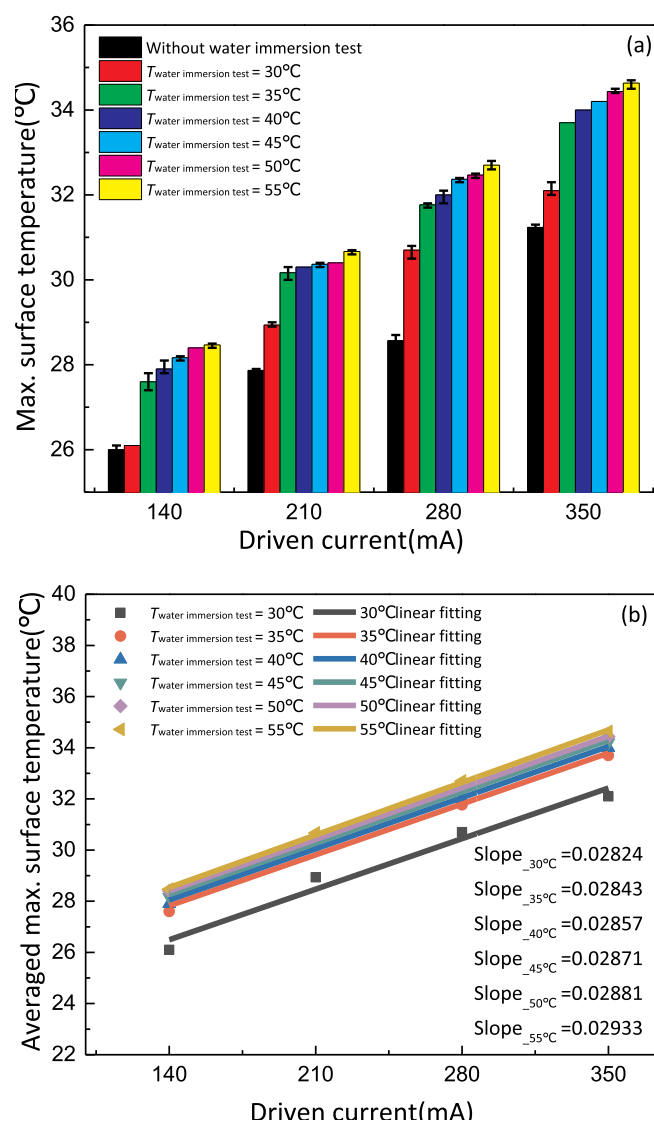


Fig. 9. (a) The maximum surface temperatures of CaAlSiN₃:Eu²⁺ red phosphor before and after water immersion tests v.s. driven current; (b) linear-fitting curve of averaged maximum surface temperature as a function of driven current. (For interpretation of the references to color in this figure legend, the reader is referred to the Web version of this article.)

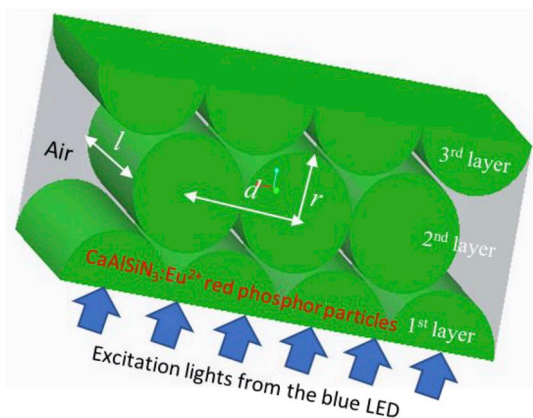


Fig. 10. A close-packed model for $\text{CaAlSiN}_3:\text{Eu}^{2+}$ red phosphor particles. (For interpretation of the references to color in this figure legend, the reader is referred to the Web version of this article.)

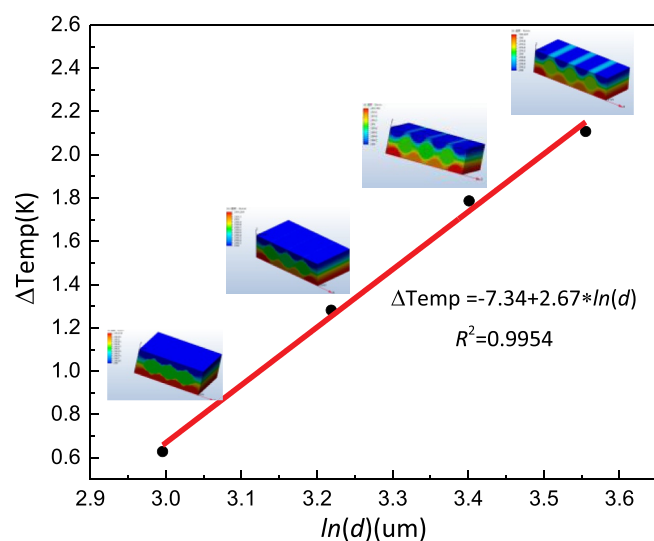


Fig. 11. The simulated temperature difference v.s. phosphor particle spacing.

test conditions we selected. A more severe test condition, including high temperature ($>150^\circ\text{C}$) and high pressure water steam, was used in Ref. [42].

The EDS images shown in Fig. 14 compares the chemical element distributions of $\text{CaAlSiN}_3:\text{Eu}^{2+}$ red phosphor particles before and after 55°C water immersion test. This is a qualitative surface scanning results of chemical element distribution, in which the brighter the image shows, the more specific chemical element it has. Meanwhile, the quantitative atomic percentages of chemical elements are shown in Table 4, which reveals that the N and Eu elements reduced and the Al and Si elements kept relatively stable. Combining the electrical conductivity measurement results, the hydrolysis reaction of $\text{CaAlSiN}_3:\text{Eu}^{2+}$ red phosphor can be assumed as a two-stage mechanism: Firstly, the Ca^{2+} and OH^- were decomposed to the water as shown in equation (5), resulting in a dramatic increase of solution's electrical conductivity (Fig. 4) and pH value [19]. Secondly, the gaseous NH_3 and solid-state $\text{CaAl}_2\text{Si}_2\text{O}_8$ and $\text{Ca}(\text{OH})_2$ were generated to make the solution's electrical conductivity stable, which also proves that the hydrolysis reaction equation proposed in Ref 42⁴² is reasonably when equations (5) and (6) are combined together.

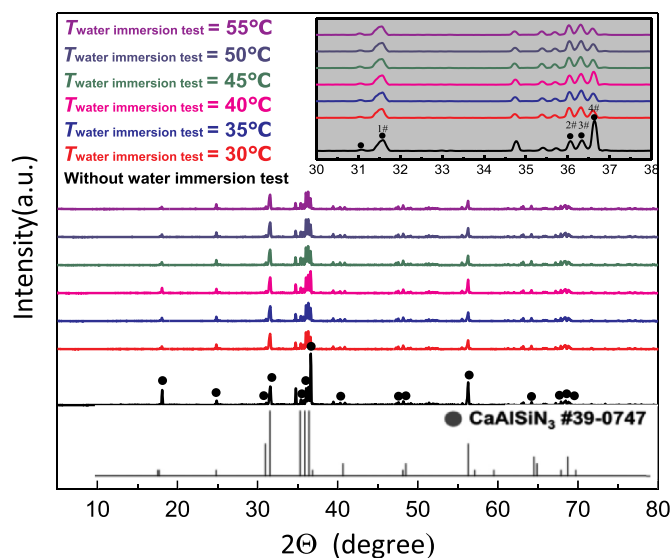
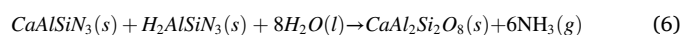


Fig. 12. XRD patterns of $\text{CaAlSiN}_3:\text{Eu}^{2+}$ red phosphors before and after water immersion test. (For interpretation of the references to color in this figure legend, the reader is referred to the Web version of this article.)

Table 3

The peak intensities at four characteristic diffraction angles.

$T_{\text{water immersion test}}/^\circ\text{C}$	Peak intensities/a.u.			
	1# $\sim 31.6^\circ$	2# $\sim 36.0^\circ$	3# $\sim 36.3^\circ$	4# $\sim 36.6^\circ$
No soaking	13339	12092	13014	36737
30	10890	12017	12732	8808
35	10678	11281	13074	9467
40	11216	11174	13082	15648
45	11057	12608	13528	10083
50	10445	12608	12807	8946
55	10312	11733	12430	7762



3.6. Hydrolysis mechanism analysis with first-principles calculation

To further understand the hydrolysis reaction mechanism in present water immersion test, a preliminary density functional theory (DFT) calculation was conducted by using the program package DMol [3]. [48] The electronic interactions were employed by using the generalized gradient approximation (GGA) with the Perdew-Burke-Ernzerhof (PBE) method [49]. Double numerical basis sets with polarization functions (DNP) were utilized. For the optimization calculations, a $5 \times 4 \times 3$ Monkhorst-Pack k -point mesh for the Brillouin zone sampling was used. The convergence criteria of optimized structures are 2×10^{-5} ha for energy, 0.002 Ha/Å for force, and 5×10^{-3} Å for displacement. The Mulliken charge analysis approach was used to calculate the charge density of the structure. Before the modelling of the hydrolysis reaction, the unit cell of CaAlSiN_3 crystal structure was optimized with 24 atoms. The positions of two Al atoms and two Si atoms are shown in Fig. 15 (a). When the unit cell was fully relaxed by employing the conjugate gradient method, the lattice constants of that were calculated as $a = 9.8871$ Å, $b = 5.7134$ Å, and $c = 5.1146$ Å. These calculated parameters are in good agreement with the previous studies [38,40].

The CaAlSiN_3 surfaces with orientation [100], [010] and [001] are observed in the experiment [50]. But it has great difficulties in simulating the surface with all those orientations, thus we chose the CaAlSiN_3 [010] surface for calculation. The weak interactions between Ca^{2+} and surrounding atoms indicate that, at the surface region, Ca^{2+} would first

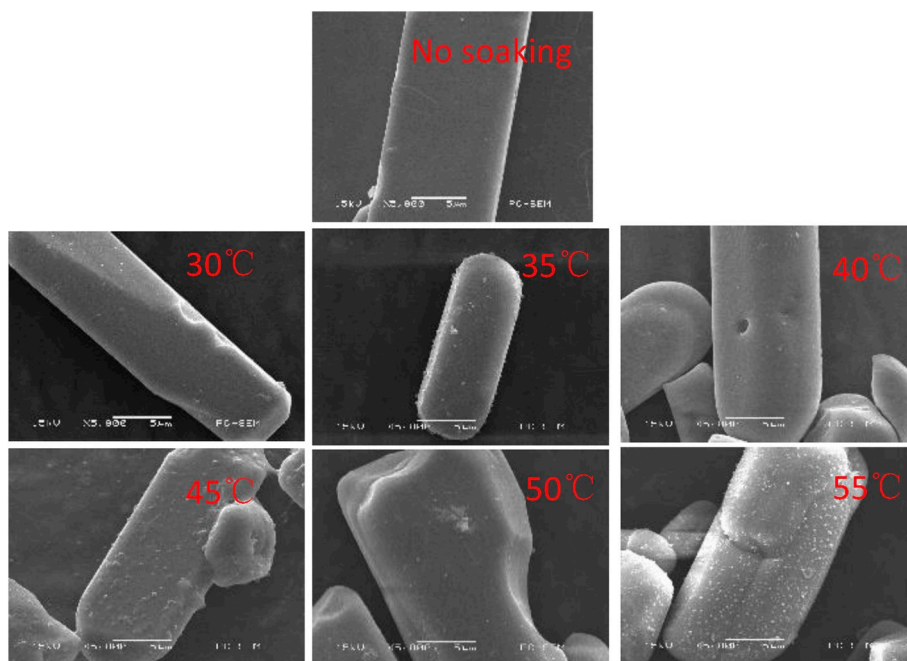


Fig. 13. SEM images of CaAlSiN₃:Eu²⁺ red phosphors before and after water immersion test. (For interpretation of the references to color in this figure legend, the reader is referred to the Web version of this article.)

diffuse into water solution before the hydrolysis reaction with water. Thus, the CaAlSiN₃ [010] surface structure, losing a Ca²⁺ at the surface, was optimized to model the surface condition before the hydrolysis reaction. In addition, the Ca²⁺ and H₂O were placed in a 15 × 15 × 15 Å³ cubic cell to obtain the equilibrium position between Ca²⁺ and H₂O. Then, the optimized Ca²⁺ and H₂O were added to the relaxed CaAlSiN₃ [010] surface structure to model the hydrolysis reaction. A thick vacuum layer (>15 Å) was added in the direction perpendicular to the CaAlSiN₃ [010] surface to ensure the minimum interaction between periodic structures, and the six bottom layers of the surface structure were fixed to model to bulk property of CaAlSiN₃, as shown in Fig. 15(b).

Fig. 16 (a) plots the optimized surface structure after hydrolysis reaction, it can be seen that the bond of H–OH in water molecular is broken, then the H⁺ is adsorbed on the surface, forming a N–H bond with length 1.027 Å. But the Ca²⁺ and OH[−] leave distantly from the CaAlSiN₃ (010) surface after hydrolysis reaction, which indicates a weak interaction between the OH[−] and CaAlSiN₃ surface. To better understand the mechanism of the reaction of H₂O on the surface of CaAlSiN₃, we plot the image of charge density difference (CDD) calculated by the following formula [51],

$$\Delta\rho = \rho_{\text{H}_2\text{O} + \text{CaAlSiN}_3} - \rho_{\text{H}_2\text{O} + \text{Ca}^{2+}} - \rho_{\text{CaAlSiN}_3 - \text{Ca}^{2+}} \quad (7)$$

where $\rho(\text{H}_2\text{O} + \text{CaAlSiN}_3)$, $\rho(\text{H}_2\text{O} + \text{Ca}^{2+})$, and $\rho(\text{CaAlSiN}_3 - \text{Ca}^{2+})$ are the total charge density of the optimized H₂O + CaAlSiN₃ structure, the equilibrium structure of Ca²⁺ and H₂O, and the isolated structure of CaAlSiN₃ losing a Ca²⁺, respectively.

The CDD image in Fig. 16(b) shows the charge transfer before and after the hydrolysis reaction of CaAlSiN₃ [010] surface. It can be seen that the H⁺ acts as a donor and provides 0.33 *e* to the CaAlSiN₃. Meanwhile, a slight charge transfer from OH[−] to CaAlSiN₃, 0.04 *e*, is also observed. Such a strong charge transfer and the close distance between H and N atoms imply that the H⁺ is chemically adsorbed on the surface via the covalent interaction. But, the slight charge transfer and relatively far distance between OH[−] and CaAlSiN₃ [010] surface show that the OH[−] is physically adsorbed on the surface via a van der Waals interaction. Since the interaction of chemisorption is much stronger than the physisorption, thus the OH[−] is much easier than H⁺ to be dissolved in water solution during the hydrolysis reaction. This would lead to a

higher concentration of OH[−] than H⁺ in water solution, which is consistent with our previous experimental results that the increased pH value in water solution after the water immersion test of CaAlSiN₃ [24]. And the simulation results also explain the above experiment phenomenon from water immersion test that an increase of solution's electrical conductivity was always detected at the initial stage of water immersion test. Therefore, the DFT calculations provide an insight into the mechanism of the hydrolysis reaction of CaAlSiN₃, which also can reasonably explain the initial hydrolysis reaction function as shown in equation (5).

4. Conclusions

To qualify the reliability of CaAlSiN₃:Eu²⁺ red phosphor used in high temperature and high humidity condition, a kinetic study with both the water immersion test and first-principles calculation is proposed in this paper to understand its hydrolysis reaction mechanism. The results show that: (1) Firstly, the water immersion test reveals that an in-situ monitored electrical conductivity of CaAlSiN₃:Eu²⁺ red phosphor water solution can be used to quantitatively calculate the phosphor's hydrolysis reaction rate, which is temperature dependent and satisfies the Arrhenius model; (2) The hydrolysis reaction at high temperature can dramatically deteriorate the emission peak intensity of CaAlSiN₃:Eu²⁺ red phosphor accompanying with an increase of its photothermal effect (3) Both experimental characterizations (i.e. the crystalline phase analysis and micromorphology and chemical element analysis), and first-principles calculation infer that the moisture driven degradation of CaAlSiN₃:Eu²⁺ red phosphor can be attributed to the initially dissolved of Ca²⁺ and OH[−], gradually crashed crystallinity of host lattice and the increased surface roughness from reaction residues. The major contributions of this study can support improving the pc-wLED&LD phosphor's reliability under high humidity usage condition, and also providing the technical guidance on the fast, accurate and cost-effective reliability assessment for pc-wLED&LD phosphors.

Declaration of competing interest

All authors declare no conflict of interest.

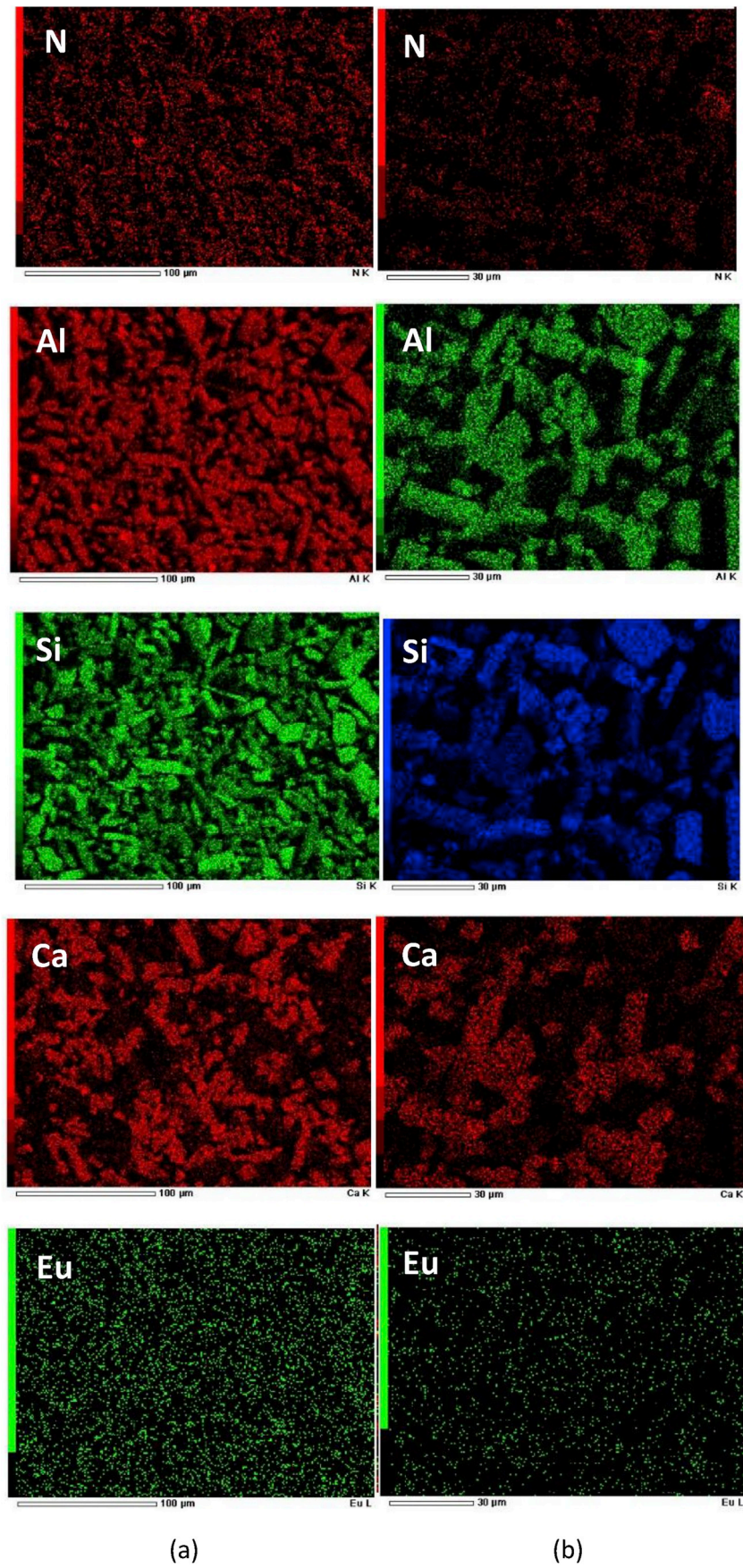


Fig. 14. EDS images of $\text{CaAlSiN}_3:\text{Eu}^{2+}$ red phosphor particles (a) before test; (b) after test at 55 °C. (For interpretation of the references to color in this figure legend, the reader is referred to the Web version of this article.)

Table 4

Atomic percentages of $\text{CaAlSiN}_3:\text{Eu}^{2+}$ red phosphors before and after water immersion test.

$T_{\text{water immersion test}}/^\circ\text{C}$	Ca/At%	Al/At%	Si/At%	N/At%	Eu/At%
Before test	14.35	31.52	28.54	20.81	0.57
30	22.41	33.04	31.99	11.45	1.13
35	19.82	33.64	30.38	15.67	0.50
40	24.01	24.78	27.61	23.40	0.21
45	11.32	37.60	33.03	17.18	0.87
50	15.38	37.69	34.11	11.81	0.90
55	28.83	27.74	31.57	11.58	0.28

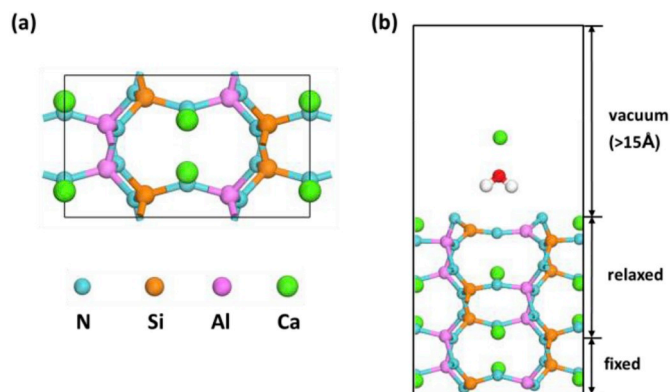


Fig. 15. (a) The crystal structure of CaAlSiN_3 . (b) The initial structure for the modelling of hydrolysis reaction.

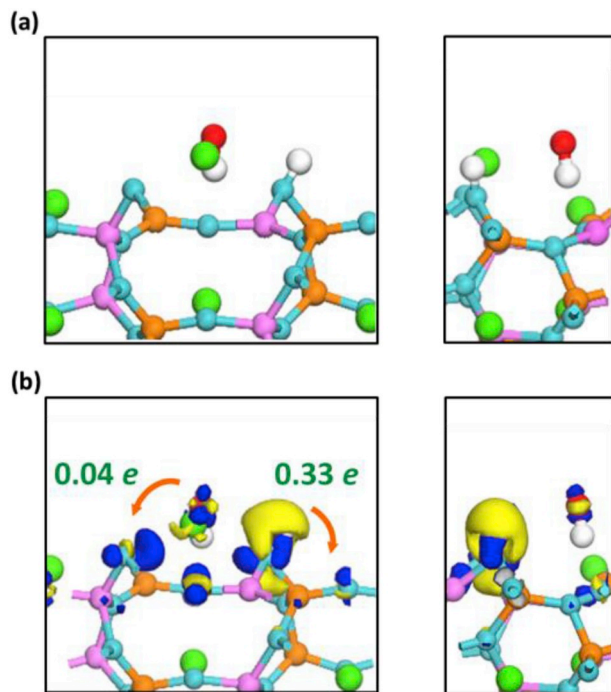


Fig. 16. (a) The optimized structure after the modelling of hydrolysis reaction. (b) The charge density difference of the $\text{CaAlSiN}_3+\text{H}_2\text{O}$ configuration. The isosurfaces are taken as $6 \times 10^{-2} e/\text{\AA}^3$. The blue areas show where the electron density has been enriched. Conversely, the yellow areas show where the density has been depleted. The direction and value of charge transfer are also plotted. (For interpretation of the references to color in this figure legend, the reader is referred to the Web version of this article.)

Acknowledgements

The work described in this paper was partially supported by the National Natural Science Foundation of China (51805147, 61673037), the Six Talent Peaks Project in Jiangsu Province (GDZB-017) and the Fundamental Research Funds for the Central Universities (2017B15014).

Appendix A. Supplementary data

Supplementary data to this article can be found online at <https://doi.org/10.1016/j.jlumin.2019.116874>.

References

- [1] W.D. van Driel, X.J. Fan (Eds.), *Solid State Lighting Reliability Part 1: Components to Systems*, Springer, 2011.
- [2] W.D. van Driel, X. Fan, G.Q. Zhang (Eds.), *Solid State Lighting Reliability Part 2: Components to Systems*, Springer, 2018.
- [3] J.J. Fan, M.G. Mohamed, C. Qian, X.J. Fan, G.Q. Zhang, M. Pecht, *Materials* 10 (2017).
- [4] J.J. Fan, K.C. Yung, M. Pecht, *IEEE Trans. Device Mater. Reliab.* 14 (2014) 564–573.
- [5] M. Cai, D.G. Yang, J.L. Huang, M.F. Zhang, X.P. Chen, C.H. Liang, S. Koh, G. Q. Zhang, *IEEE Photonics J.* 9 (2017).
- [6] C.C. Lin, R.S. Liu, *J. Phys. Chem. Lett.* 2 (2011) 1268–1277.
- [7] J. Ueda, P. Dorenbos, A.J.J. Bos, A. Meijerink, S. Tanabe, *J. Phys. Chem. C* 119 (2015) 25003–25008.
- [8] R. Hu, X. Fu, Y. Zou, X.B. Luo, *Opt. Express* 21 (2013) 5071–5073.
- [9] R. Hu, X.B. Luo, H. Feng, S. Liu, *J. Lumin.* 132 (2012) 1252–1256.
- [10] R. Hu, S. Yu, Y. Zou, H. Zheng, F. Wang, S. Liu, X.B. Luo, *IEEE Photonics Technol. Lett.* 25 (2013) 246–249.
- [11] J.H. Li, J. Yan, D.W. Wen, W.U. Khan, J.X. Shi, M.M. Wu, Q. Su, P.A. Tanner, *J. Mater. Chem. C* 4 (2016) 8611–8623.
- [12] X.Y. Huang, *Nat. Photonics* 8 (2014) 748.
- [13] R.J. Xie, N. Hirosaki, T. Takeda, T. Suehiro, *ECS J. Solid State Sci. Technol.* 2 (2013) R3031–R3040.
- [14] H.L. Liu, Y.Y. Hao, B.S. Xu, *Acta Phys. Sin.* 62 (2013).
- [15] L. Wang, R.J. Xie, Y.Q. Li, X.J. Wang, C.G. Ma, D. Luo, T. Takeda, Y.T. Tsai, R. S. Liu, N. Hirosaki, *Light Sci. Appl.* 5 (2016).
- [16] P. Singh, C.M. Tan, *Sci. Rep.* 6 (2016).
- [17] Z.H. Ma, H.C. Cao, X.J. Sun, C. Yang, X. Xi, J. Li, S. Lin, L.X. Zhao, *Phys. Status Solidi A Appl. Mater. Sci.* 216 (2019).
- [18] R. Hu, Z.Z. Du, T. Cheng, Z.X. Huang, W.Z. Liu, X.B. Luo, *J. Appl. Phys.* 118 (2015).
- [19] J.J. Fan, M.N. Zhang, X. Luo, C. Qian, X.J. Fan, A.M. Ji, G.Q. Zhang, *J. Mater. Sci. Mater. Electron.* 28 (2017) 17557–17569.
- [20] C.M. Tan, B.K. Chen, X. Li, S.J. Chen, *IEEE Trans. Device Mater. Reliab.* 12 (2012) 44–48.
- [21] M. Choi, K.H. Kim, C. Yun, D.H. Koo, S. Bin Song, J.P. Kim, *Microelectron. Reliab.* 54 (2014) 2849–2852.
- [22] C.F. Guo, L. Luan, D.X. Huang, Q. Su, Y.H. Lv, *Mater. Chem. Phys.* 106 (2007) 268–272.
- [23] W.X. Li, Z. Song, D.P. Cui, Z.G. Xia, Q.L. Liu, *J. Rare Earths* 36 (2018) 341–345.
- [24] J.J. Fan, Z. Wang, X. Luo, et al., *Rare Metal Materials and Engineering*, 2019.
- [25] X. Luo, J.J. Fan, M.N. Zhang, C. Qian, X.J. Fan, G.Q. Zhang, 18th International Conference on Electronic Packaging Technology (Icept) 2017, 2017, pp. 1331–1336.
- [26] I. Khalilullah, T. Reza, L.B. Chen, M. Placette, A.K.M.M.H. Mazumder, J. Zhou, J. J. Fan, C. Qian, G.Q. Zhang, X.J. Fan, *Microelectron. Reliab.* 84 (2018) 208–214.
- [27] Y.B. Chen, K.L. Wu, J. He, Z.B. Tang, J.X. Shi, Y.Q. Xu, Z.Q. Liu, *J. Mater. Chem. C* 5 (2017) 8828–8835.
- [28] Y.Y. Zhou, E.H. Song, T.T. Deng, Q.Y. Zhang, *ACS Appl. Mater. Interfaces* 10 (2018) 880–889.
- [29] C. Cai, J. Qian, B. Zhang, W.W. Hu, L.Y. Hao, X. Xu, Y.F. Wang, *ECS J. Solid State Sci. Technol.* 3 (2014) R169–R172.
- [30] S.L. Chung, S.C. Huang, *Materials* 7 (2014) 7828–7842.
- [31] S.X. Li, X.J. Liu, J.Q. Liu, H.L. Li, R.H. Mao, Z.R. Huang, R.J. Xie, *J. Mater. Res.* 30 (2015) 2919–2927.
- [32] G.H. Li, J.J. Chen, Z.Y. Mao, W.W. Song, T. Sun, D. Wang, *J. Mater. Sci. Mater. Electron.* 26 (2015) 10201–10206.
- [33] G.H. Li, J.J. Chen, Z.Y. Mao, W.W. Song, T. Sun, D. Wang, *J. Ceram. Int.* 42 (2016) 1756–1761.
- [34] Y.F. Yang, Y. Zhao, J.J. Chen, Z.Y. Mao, G.H. Li, J. Xu, D.J. Wang, B.D. Fahlman, *J. Mater. Sci. Mater. Electron.* 28 (2017) 715–720.
- [35] K. Uheda, N. Hirosaki, Y. Yamamoto, A. Naito, T. Nakajima, H. Yamamoto, *Electrochem. Solid State Lett.* 9 (2006) H22–H25.
- [36] K. Uheda, N. Hirosaki, H. Yamamoto, *Phys. Status Solidi A Appl. Mater. Sci.* 203 (2006) 2712–2717.
- [37] M. Mikami, K. Uheda, N. Kijima, *Phys. Status Solidi A Appl. Mater. Sci.* 203 (2006) 2705–2711.
- [38] Z.Y. Wang, B. Shen, F. Dong, S.Y. Wang, W.S. Su, *Phys. Chem. Chem. Phys.* 17 (2015) 15065–15070.

- [39] S.X. Li, X.J. Liu, R.H. Mao, Z.R. Huang, R.J. Xie, RSC Adv. 5 (2015) 76507–76515.
- [40] S. Jang, J. Im, B.K. Bang, C.H. Kim, H. Chang, K.J. Kong, RSC Adv. 5 (2015) 39319–39323.
- [41] J. Ueda, S. Tanabe, K. Takahashi, T. Takeda, N. Hirosaki, Bull. Chem. Soc. Jpn. 91 (2018) 173–177.
- [42] J. Zhu, L. Wang, T.L. Zhou, Y.J. Cho, T. Suehiro, T. Takeda, M. Lu, T. Sekiguchi, N. Hirosaki, R.J. Xie, J. Mater. Chem. C 3 (2015) 3181–3188.
- [43] Y. Li, L.L. Hu, B.B. Yang, M.M. Shi, J. Zou, J. Mater. Sci. Mater. Electron. 28 (2017) 19155–19163.
- [44] S.X. Li, Q.Q. Zhu, L. Wang, D.M. Tang, Y.J. Cho, X.J. Liu, N. Hirosaki, T. Nishimura, T. Sekiguchi, Z.R. Huang, R.J. Xie, J. Mater. Chem. C 4 (2016) 8197–8205.
- [45] D.S. Jo, K. Senthil, Y.H. Song, T. Masaki, D.H. Yoon, J. Ceram. Process. Res. 15 (2014) 259–261.
- [46] P. He, N. Zhang, S.Q. Man, Adv. Mater. Mach. Electron. Ind. (2017) 1820.
- [47] J.W. Li, T. Watanabe, H. Wada, T. Setoyama, M. Yoshimura, Chem. Mater. 19 (2007) 3592–3594.
- [48] B. Delley, J. Chem. Phys. 92 (1990) 508–517.
- [49] John P. Perdew, Kieron Burke, Matthias Ernzerhof, Phys. Rev. Lett. 77 (18) (1996) 3865–3868.
- [50] Shuxing Li, Daiming Tang, Zifeng Tian, Xuejian Liu, Takashi Takeda, Naoto Hirosaki, Fangfang Xu, Zhengren Huang, Rongjun Xie, J. Mater. Chem. C 5 (2017) 1042–1051.
- [51] O. Leenaerts, B. Partoens, F.M. Peeters, Phys. Rev. B 77 (2008).